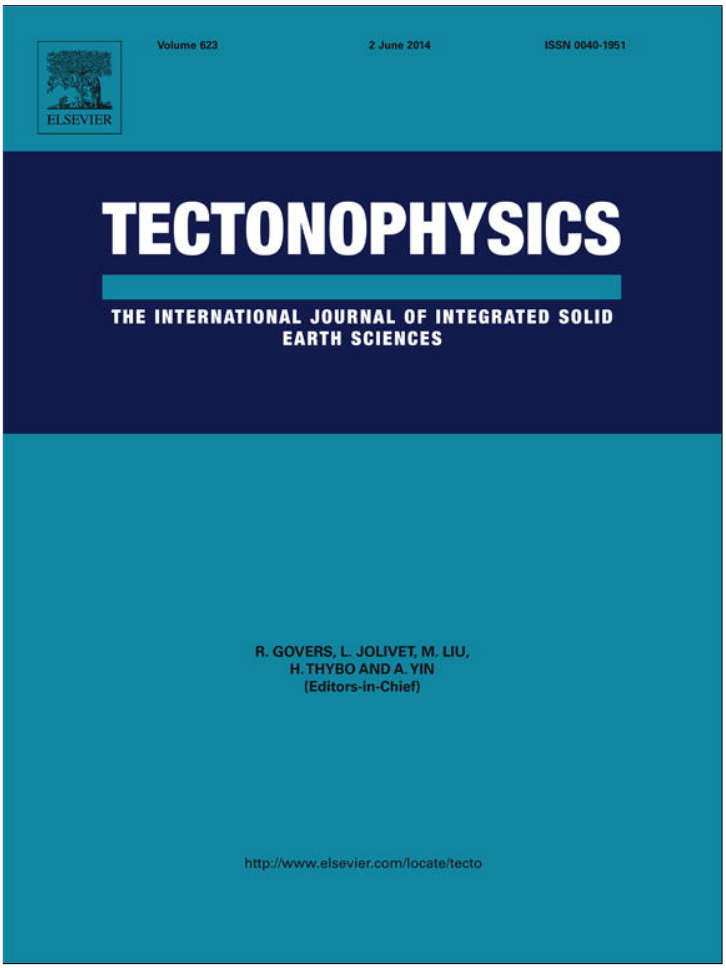

Tectonophysics 623 (2014) 14–22

Contents lists available at ScienceDirect

Tectonophysics

journal homepage: www.elsevier.com/locate/tecto

Determining the geometry of the North Anatolian Fault East of the Marmara Sea through integrated stress modeling and remote sensing techniques

Bobak Karimi [a,*], Nadine McQuarrie [a], Jeen-Shang Lin [b], William Harbert [a]

[a] Department of Geology & Planetary Science, University of Pittsburgh, 4107 O'Hara Street, SRCC, Room 200, Pittsburgh, PA 15260-3332, United States
[b] Department of Civil & Environmental Engineering, University of Pittsburgh, 3700 O'Hara Street, Pittsburgh, PA 15261, United States

ARTICLE INFO

Article history:
Received 16 September 2013
Received in revised form 12 March 2014
Accepted 15 March 2014
Available online 22 March 2014

Keywords:
North Anatolian Fault (NAF)
Stress modeling
Paleostress
Lineament analysis
Active fault geometry
Finite element model

ABSTRACT

The 1200 km long North Anatolian Fault (NAF) is part of an east–west trending dextral shear zone (NAF system), along the boundary between the Anatolian and Eurasian plates, that widens to the west. This widening zone of deformation complicates potential earthquake rupture paths and highlights the importance of understanding the geometry of active fault systems. In the central portion of the NAF system – just west of the town of Bolu – the NAF splits into two major faults: the northern and southern strands. These two faults diverge, almost converge, and then diverge again to border the Marmara Sea. Earthquake data from the region where the two faults converge indicate that they may be linked by an active fault. We model the active fault geometries with and without the linking fault to explore its impact on the output regional stress field (from a finite element model). These results are compared to focal mechanism records and lineament analyses to determine which geometry best simulate the stress field in a regional model. Our results show that a linking fault between the northern and southern strands of the NAF system is necessary to best match the primary stress orientations of the model with the maximum paleostress orientations inferred from deformation patterns, and observed in earthquake focal mechanisms. Furthermore, the linking fault should be a significant component in future models of the NAF system within the region.

1. Introduction

Due to the effect of fault geometry on modeled stress and strain fields, accurately representing the active fault geometry is a critical component of the modeling process (Bilham and King, 1989; Lesne et al., 1998). Longer, linked faults play host to the majority of earthquakes – particularly high magnitude earthquakes – in a fault system (Barka and Kadinsky-Cade, 1988; Slemmons and Depolo, 1986), and are the most influential in the development of the regional stress and strain field (Bilham and King, 1989; Lesne et al., 1998; Schwartz and Coppersmith, 1986). In strike-slip systems, short extensional faults linking echelon fault segments allow for long-term transfer of fault slip, thus affecting the stress field distribution, and may also act as kinetic barriers impeding or arresting rupture propagation (King, 1986; King and Nábělek, 1985; Sibson, 1986). Fault geometry is sometimes hard to observe as a trace on the surface when there is little to no topographic expression, or if the fault has been covered by young sediments. In this study, we examine the relationship between fault geometry, and numerically determined stress and strain fields along a strike-slip fault in Turkey by utilizing a methodology adapted from McElfresh et al. (2002).

The North Anatolian Fault (NAF) system has seen several devastating and high magnitude earthquakes, particularly in the Marmara Sea region (Bohnhoff et al., 2013; Parsons, 2004). The 1999 earthquake of August 17th was of particular note for being the largest recorded earthquake in Turkey by modern digital networks (Özalaybey et al., 2002) with a devastating death toll of over 17,000 people (Scawthorn and Johnson, 2000). In the region impacted by the 1999 earthquake, the through-going NAF splits into two strands just west of the town of Bolu (Barka et al., 2002; engör et al., 2005; Hergert and Heidbach, 2010): the Düzce and Karadere faults (NE portion of the northern strand), which we refer to as a single fault called the Düzce–Karadere and the Mudurnu fault (SE portion of the southern strand) (Fig. 1). Two potential geometries of the active through-going strands of the NAF are proposed. One active fault geometry suggests that two strands almost converge (west of Bolu) and then diverge as distinct fault traces (Fig. 1B) (Akyüz et al., 2002; Barka et al., 2002). The fault strands continue on to border the Marmara Sea in the north and south respectively (Fig. 1B): the northern strand as the Izmit fault, and the southern strand as the Iznik fault (Armijo et al., 2002; engör et al., 2005). The second

* Corresponding author.
E-mail addresses: bok10@pitt.edu (B. Karimi), nmcq@pitt.edu (N. McQuarrie), jslin@pitt.edu (J.-S. Lin), harbert@pitt.edu (W. Harbert).

http://dx.doi.org/10.1016/j.tecto.2014.03.015
0040-1951/

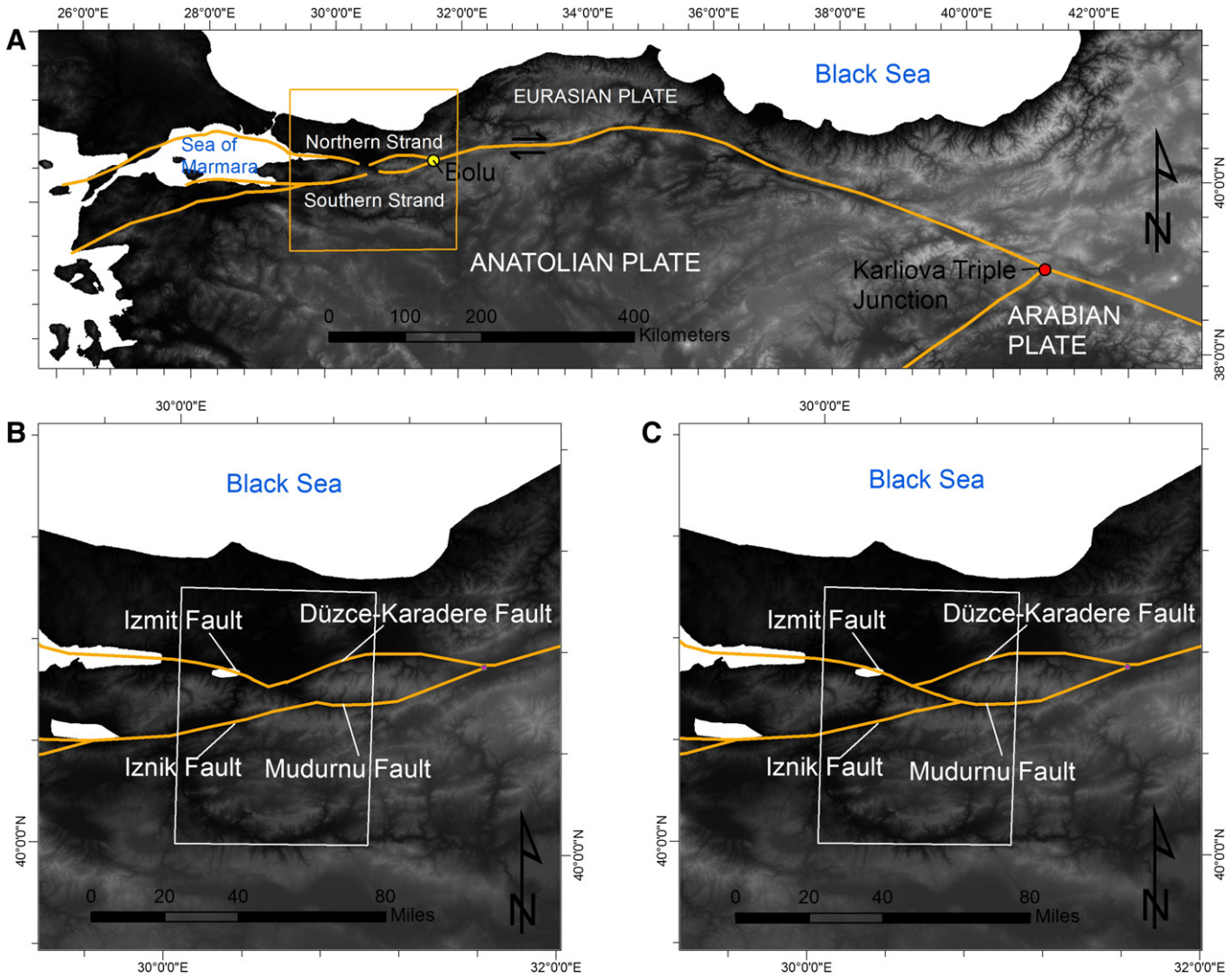

Fig. 1. A) Tectonic setting of the NAF. The NAF splits near the town of Bolu and continues on as two strands around the Sea of Marmara; B) possible fault geometry where the northern and southern strands converge, then diverge (model 1); C) second possible fault geometry where the two strands are linked (model 2).

geometry is similar, except that the southern and northern faults described above are linked by a fault through the Mudurnu valley (Fig. 1C). A study of fracture zones attributed to major earthquakes of the 20th century by Koulakov et al. (2010) shows this link, as does previous work to understand stress transfer on the NAF by Stein et al. (1997). Studies of dextral displacement of Eocene volcanic rocks in the region between the northern and southern also imply an extensional linking fault (Armijo et al., 1999; Hisarli et al., 2011; Yılmaz et al., 1997). Seismic data from the Mudurnu valley show a normal sense of motion, indicating that the link may be an extensional fault between two major echelon fault segments (Mudurnu and Izmit faults) (Heidbach et al., 2008; International Seismological Centre, 2011; Neugebauer et al., 1997). A 100 year record of earthquakes (KOERI-UDIM, 2012) clusters around the northern strand, but also illustrates that the Mudurnu valley is seismically active, suggesting a connecting fault and supporting the second geometry (Fig. 2A). Additionally, it is proposed that the rupture of the 1967 M7.1 Mudurnu earthquake, the most recent of a series of historical earthquakes at its location (Palyvos et al., 2007), reached Lake Sapanca (along the Izmit fault) as distributed deformation (Ambraseys and Zatopek, 1969; Muller et al., 2003). Elevation data from a 10 meter Digital Elevation Model (DEM) – courtesy of the (GLCF) (USGS, 2008) – highlight pronounced topographic features that are a result of the southern and northern fault strands. The southern strand is located along narrow river valleys, while the northern strand controls the sharp transition from high to low topography (Fig. 2B). This fault-controlled topography has led to the inference of no connecting fault between the two segments. A potential linking fault from the Mudurnu fault to the Izmit fault can be traced through a narrow river valley, but loses any topographic expression as it nears the northern strand. Previous studies evaluating earthquake ruptures on this portion of the NAF system identify the Mudurnu fault in the southern Mudurnu valley, but terminate the fault trace before it links to the northern strand (Akyüz et al., 2002; Barka et al., 2002). This raises a question regarding the significance of a fault linking the two strands as part of the through-going NAF geometry within the region, and which geometry will best duplicate the regional stress and strain in geophysical models.

Determining the geometry of the active fault system would allow for more detailed and accurate models of the stress accumulation along the NAF, one of the world's largest active strike-slip faults. Stress accumulation can be used to define a region with a higher probability for seismic risk (Bowman and King, 2001; Stein et al., 1997). This study utilizes simplified fault geometries and friction values, surficial geology, rock physics parameters, and GPS velocities as model inputs. We created simplified two-dimensional models for each of the fault geometries and processed them with a finite element method to evaluate primary stress orientations for the region. The stress orientations from the two models are compared to lineament analyses and a record of focal

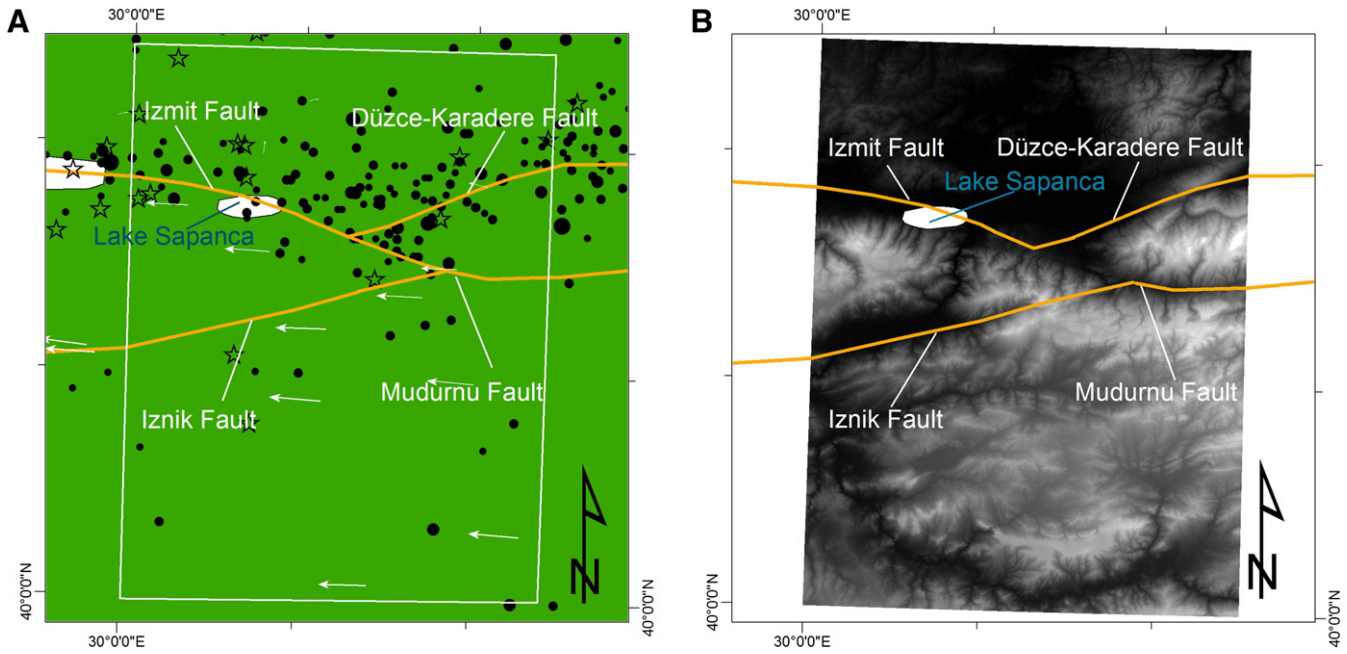

Fig. 2. A) A 100-year record of earthquakes (KOERI-UDIM, 2012) along the NAF sized according to magnitude with GPS vectors as arrows (Ozener et al., 2009), and location of focal mechanism data (Heidbach et al., 2008; International Seismological Centre, 2011) as stars. B) A DEM of the region (USGS, 2008). The linked fault can partially be traced along a river valley, but as it approaches the northern strand, the nature of the link remains ambiguous.

mechanisms from the region to determine which geometry of active faults best reproduces the inferred stress field within an 85 km wide by 111 km long region centered around the Mudurnu valley. We evaluate the accuracy of the generated stress field from the finite element model (FEM) by comparing it to regional focal mechanisms, and inferred paleostress orientations determined from relating lineaments to potential structures.

We utilize PyLith – a finite element code tectonic deformation software – (Aagaard et al., 2012) to calculate the stress field in the region of interest for both models and compare the σ_1 orientation frequency and magnitude of the stress field to the principal stress orientations suggested from lineament analyses and focal mechanisms. The overall goal of this study is to identify the active fault geometry of the NAF within the region of interest, which best duplicates the regional stress field as determined from focal mechanism data and lineament analyses.

2. Geologic background

The NAF forms the most prominent part of a strike-slip dominated belt of deformation between the Eurasian and Anatolian plates (engör et al., 2005). It extends from the junction of the NAF at the East Anatolian Fault (EAF) near the town of Karliova Turkey (Fig. 1) to the north Aegean region (engör et al., 2005) nearly 1200 km, paralleling the southern margin of the Black Sea. East–west widening of a dextral shear zone associated with the NAF system continues across the northern Aegean sea, broadens across the northern and central mainland parts of Greece (the Grecian Shear Zone) (engör, 1979), and is postulated to link up with the Hellenic subduction zone (Dewey and engör, 1979; McKenzie and Jackson, 1983). The NAF system is mostly contained within late Paleozoic to early Tertiary age Tethyan accretionary complexes (engör and Natal'in, 1996), which also widen from east to west (engör et al., 2005). The accretionary complex is bound by more resistant pan-African and Hercynian magmatic or metamorphic assemblages (Kröner and Stern, 2004): the Menderes and Kirşehir Massifs to the south, and the Istanbul zone and Eastern Pontides to the north (engör et al., 2005; Yılmaz et al., 1997). Magnitudes of fault displacement are not the same along the through-going NAF and generally decrease from east to west (engör and Canıtez, 1982; engör et al., 2005; Hubert-Ferrari et al., 2002). This implies that total displacement must be taken up by smaller faults within the greater NAF system that are not part of the through-going NAF. In addition, the age of fault initiation is older in the east than the west (engör et al., 2005). The bifurcation of the NAF west of Bolu is interpreted to be a result of westward widening in the zone of deformation that accompanied the westward development of the NAF. The Pleistocene northern strand borders the northern shores of the Marmara Sea, while the more poorly-defined late Miocene southern strand marks the southern sea edge (engör et al., 2005), and additionally splits and extends through the Bursa graben (Armijo et al., 2002). engör et al. (1985) and Le Pichon et al. (2003) note that the southern strand has yet to materialize a through-going main fault, and appears "fragmented". The complexity of such fragmentation can be seen within the Mudurnu valley region of which we are modeling.

3. Stress modeling of the region

3.1. Fault parameters

A wide range of proposed friction coefficients (μ) have been suggested for the NAF (Hergert and Heidbach, 2011; Jiménez-Munt et al., 2006; Kasapoglu and Toksöz, 1983; Provost et al., 2003; Stein et al., 1997). Provost et al. (2003) created a 3D mechanical model of the NAF and determined the friction coefficients ($\mu = 0.05$ to $\mu = 0.1$) necessary to match the calculated velocity field to the GPS velocity field. Stein et al. (1997) determine that the friction is $\mu = 0.75$ based on laboratory rock experiments, but also consider moderate pore pressure ($B = 0.5$) which makes the effective friction (μ') 0.4. Early two-dimensional, plane-stress, finite element modeling of the NAF by Kasapoglu and Toksöz (1983) resulted in the faults locking at $\mu = 0.4$. This agrees with the thin-shell finite element tectonic model of the Mediterranean proposed by Jiménez-Munt et al. (2006) who also predict that a very low friction (0.05) on the NAF is necessary to match the Anatolian block rotation seen by GPS measurements. Based on observations that large-offset plate boundary faults are weak, Hergert and Heidbach (2011) employ $\mu' = 0.05$ in their model of the

NAF system in the Marmara Sea. With so many discrepancies regarding the value of friction coefficient for the NAF, we use $\mu' = 0.4$, because it most closely matches experimentation by Byerlee (1978) while also considering a pore pressure value of 0.5. This value is applied to all the faults within the region in both models.

3.2. Geometry and rock properties

The faults defining the main strands of the NAF within our study area are nearly vertical (Ben-Zion et al., 2003) with strike-slip motion. As mentioned in Section 1, two possible orientations of the active fault geometries exist within the region of interest: (Model 1) the two strands as distinct fault traces which don't interact west of Bolu, converge from east to west, but then diverge near the center of the region of interest and continue on to border the Marmara Sea in the north and south respectively (Armijo et al., 2002; engör et al., 2005), or (Model 2) that the southern strand links up with the northern fault through the Mudurnu valley (Öztürk et al., 2009). West of the Mudurnu valley, both models are identical as the northern strand and southern strands continue on to border the Marmara Sea (Fig. 3).

We model the geometry of two distinct faults as boundaries which separate three distinct blocks/zones within the region of interest: the Istanbul zone north of the northern strand which is part of the Eurasian tectonic plate, the Armutlu–Almaçik zone between the two strands, and the Sakarya zone south of the southern strand (names adapted from Yılmaz et al. (1997)) (Fig. 3). Each zone has distinct rock types exposed at the surface, which we use to determine average densities and seismic velocities – using empirical relationships – as inputs into our models. A breakdown of the surficial geology within each zone is provided in Table 1.

Each block's density was calculated by weighting the general densities of the three rock types by their percentage of block area: 2775 kg m^{-3} for igneous rocks (Bell, 2007), 2400 kg m^{-3} for sedimentary rocks (Boyd, 2003), and 2800 kg m^{-3} for metamorphic rocks (Boyd, 2003). The densities calculated for each block were then used to extract compressional wave velocities (V_P) from the Database of Global Rock Properties by Dalhousie University/Geological Survey of Canada High Pressure Laboratory (DU/GSC, 2001). We used the V_P values for 10 MPa, as the 2-D model addresses the surface (near surface) geology, and we can assume a low confining pressure near the surface. From these compressional velocities we were able to calculate the shear wave velocities (V_S) using a V_P/V_S ratio of 1.7, which is the prescribed ratio for hard (zero-porosity) rocks (Barton, 2007). The empirically determined seismic velocities indicated a high-velocity for the Armutlu–Almaçik block relative to the Istanbul block, which is supported by local earthquake tomography by Koulakov et al. (2010). The resulting densities, V_P and V_S of each region were applied to their respective blocks in the model for processing with a finite element method.

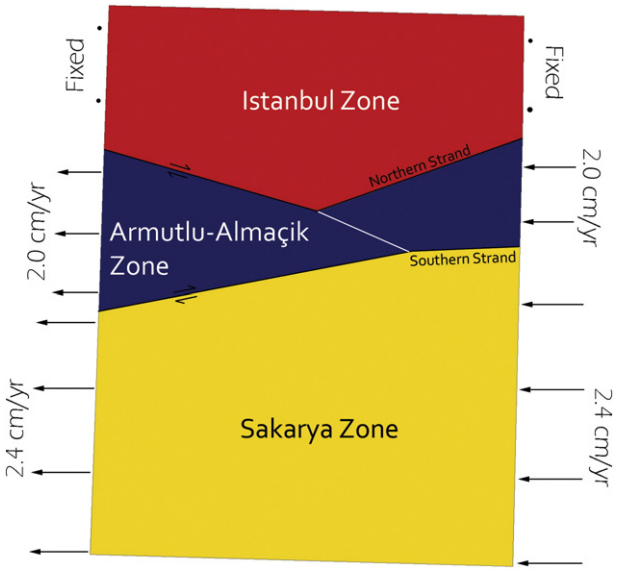

Fig. 3. Simple model of the region of interest depicting the three zones, and the two strands of the NAF separating them. The white line (fault) connecting the two strands is the difference between Model 1 (without) and Model 2 (with).

3.3. Plate motions

The NAF, together with the conjugate East Anatolian Fault (EAF), accommodates the westward extrusion of the Anatolian plate toward the Aegean subduction zone (Hubert-Ferrari et al., 2008). The NAF and EAF meet near the town of Karliova at what is known as the Karliova triple junction of the Anatolian plate, the Eurasian plate, and the Arabian plate (Fig. 1A). Lateral forces acting upon the Anatolian plate include the NNW motion of the Arabian plate at its eastern flank, the northern motion of the African plate in the south and west (where it subducts beneath the Anatolian plate at the Cyprus and Hellenic trenches), and the fixed Eurasian plate in the north. The westward extrusion of the Anatolian plate likely started some 10–12 Ma during a late phase of collision between Arabia and Eurasia (Dewey et al., 1986; Hubert-Ferrari et al., 2008; McQuarrie et al., 2003) and initiating motion along the NAF (Barka, 1992; engör et al., 1985). From GPS data, the Anatolian plate exhibits northwest motion along the East Anatolian Fault (EAF), and rotates counterclockwise to an orientation of southwest in the south Aegean region (McClusky et al., 2000; Reilinger et al., 2006). Current block motions of the Anatolian plate are 24 mm/yr in the central plate to 30 mm/yr in the SW part of the plate at the Hellenic trench (Gülen et al., 2002; McClusky et al., 2000; Reilinger et al., 2006).

Within the region of interest, the motions of each zone described in Section 3.2 were determined from GPS campaigns conducted in Turkey. GPS measurements have been carried out at both campaign and permanent geodetic control points to measure/monitor crustal movements (Ergintav et al., 2002; McClusky et al., 2000; Ozener et al., 2009; Reilinger et al., 2006). We use the horizontal GPS velocities in a Eurasia-fixed reference frame of Ozener et al. (2009). In this reference frame the Istanbul zone is on the fixed Eurasian plate (0.0 cm/yr), the Armutlu–Almaçik zone moves westward at 2.0 cm/yr, and the Sakarya zone at 2.4 cm/yr west. These rates are used to push/pull the blocks past one another.

3.4. Simplified model

We simplified the potential fault geometries based on existing geologic maps and marked changes in topography identified on a DEM. The two potential geometries are identical except for the addition of a fault connecting the southern to northern strands at their bends in Model 2 (Fig. 3). Each zone is prescribed a density, P-wave velocity, and S-wave (see Table 1). The northern and southern boundaries of the models are prescribed with roller conditions, and using the GPS velocities for each zone, the blocks are both pushed on their eastern boundary and pulled on their western boundary at their respective rates.

4. Model processing

We use PyLith (Aagaard et al., 2012), to process the models using finite elements. A triangular mesh over the region of interest was created with a grid spacing of 5 km along the outer boundaries and a finer grid of 2 km near the faults. The grid spacing is used as input to create a finer triangular mesh near the faults, which grades into a coarser mesh towards the outer boundaries. The models are processed using the rock physics and fault parameters described in Section 3, and the block's respective velocities are applied as quasi-static Dirichlet

Table 1
Surficial geology seen within the region of interest for each block and rock physics parameters–density, P-wave velocity, and S-wave velocity determined for the three blocks/zones. The Istanbul Zone is mostly softer sedimentary rocks, the Armutlu–Almaçik zone is harder metamorphic and igneous packages, and the Sakarya Zone is mostly sedimentary units, but there are metamorphic and volcanic units present.

Zone	Surficial geology	Density [kg/m^3]	Vp [m/s]	Vs (1.7) [m/s]
Istanbul	Devonian to Quaternary sedimentary units	2409	2323.9	1367.0
Armutlu–Almaçik	Nearly equal distributions of early Cenozoic sedimentary units, Paleozoic–Mesozoic metamorphic rocks, and Paleozoic–Early Cenozoic igneous rocks	2476	2913.9	1714.1
Sakarya	Mostly paleogene sedimentary units, some Paleozoic–Mesozoic metamorphic rocks, and Paleozoic igneous rocks	2501	3134.1	1843.6

boundary conditions on the east and west bounds of the blocks. Once the friction is overcome, the blocks slip along the faults at a steady rate. The models are processed for a thousand years, at a five year interval, to allow the stress field to develop enough to cause slip along all the faults while avoiding large distortions within the model area due to displacements.

From the model we calculate the orientation and magnitude of the principal stresses at the center of each triangular cell. From this, rose-diagrams of σ_1 orientation frequencies for the two models were plotted to extract a general sense of the maximum principal component trends for the region (Fig. 4). For model 1 (Fig. 4A), the largest peak associated with σ_1 can be seen at the interval from 055°–060°, with a second, almost equally large peak at 115°–120°. For model 2 (Fig. 4C), the largest peak can be seen at 120°–125°, with a second large peak at 100°–105°. Weighting the principal stress orientations by their respective magnitudes (as absolute values), we see that model 1 maintains its first strong peak, but the second peak appears at 125°–130°, with a minor peak at 90°–105° (Fig. 4B). This 'shift' in the location of the

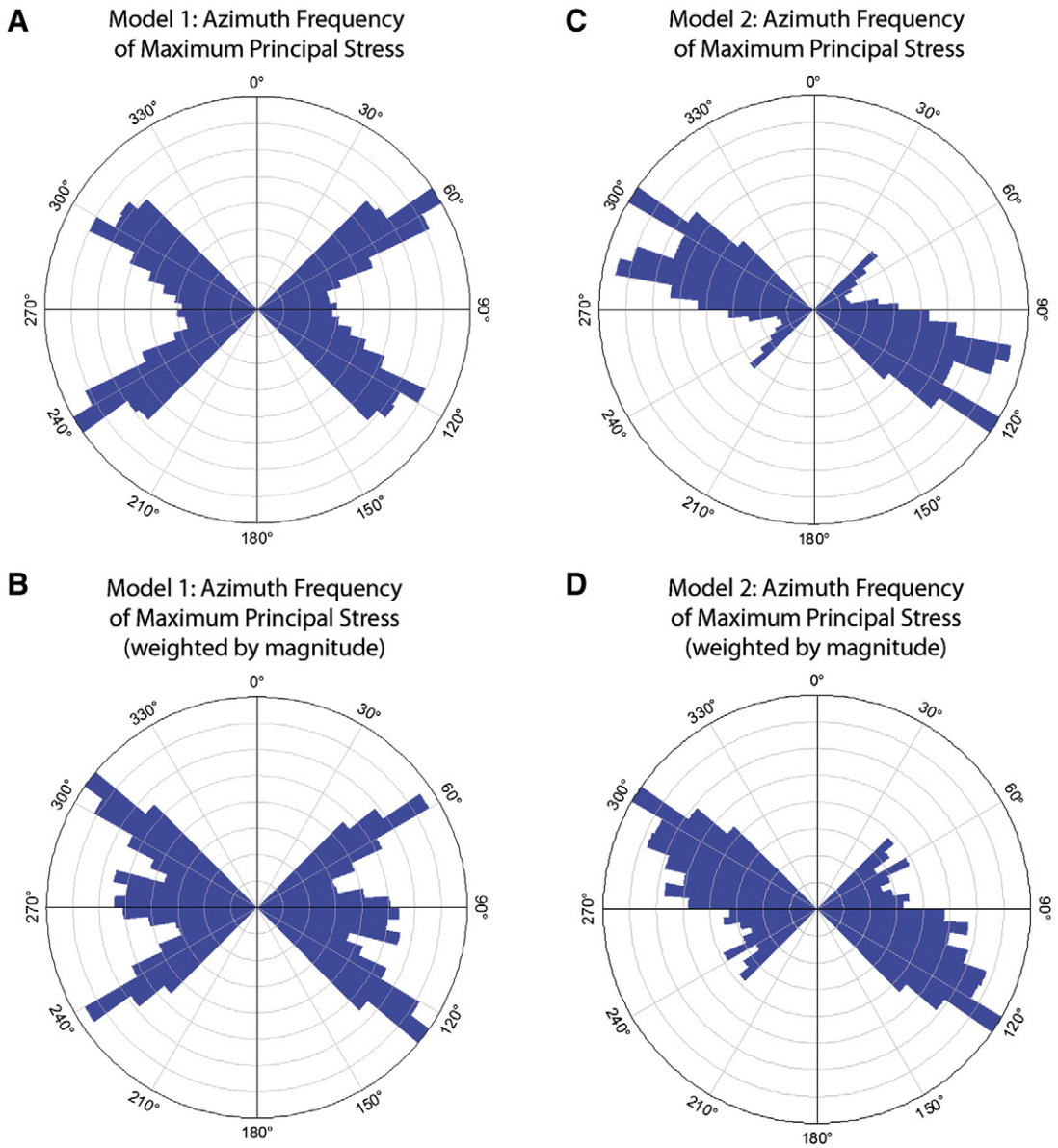

Fig. 4. Rose diagrams depicting frequency and magnitude-weighted frequency of modeled azimuths of the maximum principal stress for model 1 (A, B) and model 2 (C, D). North is at 0°.

peaks is still within the same general azimuthal region ±10°, except for addition of a 3rd, minor peak. Model 2 maintains its predominant peak, but the second peak becomes less prominent (Fig. 4D).

5. Inferring maximum paleostress orientations

Tectonic features such as faults and fractures may exert a strong control on topographic patterns due to these features creating pathways for weathering and erosion. Using digital imagery, we can highlight topographic lineaments and evaluate the potential control of tectonic induced deformation on topography. Tectonic features that may strongly influence topographic patterns include fault, large fracture systems and joints. These linear features can be mapped using digital imagery. Lineament mapping was manually performed using two sets of images: a 10-meter Digital Elevation Model (DEM) of Universal Transverse Mercator (UTM) zone 36 N courtesy of the Global Land Cover Facility (GLCF) (USGS, 2008), and an Advanced Spaceborne Thermal Emission and Reflection radiometer (ASTER) product (AST14DMO) to highlight lineament patterns. The 10-meter DEM of the region was processed by applying hill-shades to highlight topographic changes. The hill-shades were performed at a 45° vertical sun-angle, as linear features are most evident at this angle, and the azimuthal direction of the incoming solar radiation was rotated around the image at 45° increments. For the ASTER image, the bands with the highest spectral resolutions (15 m) are necessary to use in image processing and lineament picking — specifically band 3 N in the Very-Near InfraRed (VNIR) region. A directional filter was applied at 45° increments, creating a series of filtered images. The lineaments picked in these images specifically highlight differences in surface feature Digital Number (DN) values, which vary between materials. These DN value differences should highlight the main structures (such as fault displacement which juxtaposes two unique materials), and larger stream valleys, but also could further emphasize smaller scale linear features that may not show up in the resolution of the DEM, such as fluvial systems that do not exhibit prominent topographic valleys, but may take advantage of fractures and joints.

Lineaments were manually picked for both sets of images, allowing us to preferentially pick lineaments that are not man-made structures such as roads or railways. While there may be lineaments picked that do not have a tectonic source, they are outnumbered and outweighed by lineaments which are parallel to mapped faults (identified on geologic maps) (Akşay et al., 2002). To account for any curvature of lineaments we split each line into 10 sections and calculated the azimuth for each of those sections. Following this, an average azimuth and standard deviation were calculated for the orientation of each line. A very high majority of lineaments from both images had a standard deviation close to zero, but few exhibited higher deviations. The results of the average azimuths were plotted on rose diagrams (Fig. 5). Work by Hisarli et al. (2011) on Eocene volcanic rocks indicated that there was counterclockwise rotation of the eastern half of the Armutlu-Almaçik block (Almaçik) of 22.3° and 17.7° on the western half (Armutlu). We evaluated the impact of these rotations on the lineament analysis, and found that there were no changes to the prominent features in the rose plots of the lineament analyses.

The DEM lineament analysis results of orientation frequency (Fig. 5A) has its highest peaks between 80° and 90°, which match the primary orientations of faults mapped within the region. Additionally, there is a region of strong frequencies between 60° and 130° with the most predominant peaks at 60°–65° and 125°–130°. Without knowing if any faults within the region are reactivated structures, we assume that the structures that are reactivated are the ones optimally orientated in the driving stress field. Additionally, we assume that the largest peak is indicative of the orientation of major strike-slip faults, and secondary peaks are likely to be associated with Riedel shear features such as R-shears, R′-shears, P-shears and extensional fractures. With this geometry, the maximum principal stress is 45° clockwise (for right-lateral motion) from the main faults and intersects two populations of lineaments interpreted to represent R-shears and R′-shears that are characteristic of strike-slip faulting (Davis, 1999; Riedel, 1929; Wilcox et al., 1973). Under this assumption, σ_1 would be at about 125°–135°. This inferred stress orientation overlaps with a secondary peak (125°–130°), that is at an appropriate orientation to represent extensional fracturing. By weighting the lineaments according to their length (Fig. 5B), the dispersal of high frequencies disappears and we are left with a very strong feature trending 80°–85°, tightening our σ_1 orientation estimate to 125°–130°. The secondary peak, which corresponded with σ_1 almost disappears, which argues that if these are extensional fractures they are small and frequent. Plotting the location of our proposed extensional fractures on topographic and geologic maps indicates that they are oriented in stream valleys and around the edges of basins within the region. We propose that the 80° feature is the "main fault" (MF) orientation and plot the potential orientation of Riedel shears (Fig. 5A/B); with R-Shears at 100°, R′-shears at 160°, and P-shears at 75°. Both the average frequency as well as the frequency weighted by length show peaks in potential orientations of R and P shears. The presence of orientations corresponding to these shears helps validate the resolved orientation of σ_1.

The secondary peak at 60°–65° remains in both the unweighted and weighted cases (Fig. 5A/B), and does not correspond to any expected tensional or Riedel shear features. Since the lineaments oriented 60°–65° are less pronounced in the weighted rose plot (Fig. 5B), we analyze the distribution of these features, and additionally compare their orientation to mapped fault data. The DEM lineaments with this orientation are not centered in a particular region, and correspond to ridges and valleys that run nearly parallel to the Düzce–Karadere fault, the fault on the south east edge of the Istanbul zone (Fig. 3). Mapped faults indicate that this orientation further corresponds with southwest trending step-over portion of faults within the region.

Fig. 5C depicts the rose plot of the frequency average orientation of lineaments picked from the ASTER image. The ASTER image covered approximately a quarter the size of the DEM image near the center of the region of interest, but highlighted a greater number of lineaments ($n = 1835$ versus $n = 1461$ for the DEM). This lineament density increase is due to the smaller pixel size and DN value differences being highlighted rather than topography. Between 10° and 105° there is a block of peaks, with major peaks at 70°–85° and 55°–65°. The peak synonymous with the trend of mapped faults, 70°–85°, would predict an orientation of σ_1 between 115° and 130°. The second major peaks are associated with portions of the NE–SW trending faults and step-over components of other faults. To a first order, all major peaks (and σ_1 orientations), overlap with those identified in the DEM lineament analysis. Weighting the results by the lengths of the lineaments (Fig. 5D), we continue to see a very strong feature at 70°–85°, but the second feature at 55°–65° diminishes to background levels. The possibility of Riedel shears is also present in the ASTER lineament data, but is more uncertain (Fig. 5C/D).

Combining the frequency of lineament orientations from the two datasets for the region (Fig. 5E), we can see peaks at 60°–65°, 75°–85°, and 125°–130°. The peak at 125°–130° is once again attributed to small extensional fractures parallel to σ_1. When we weight the combined lineaments by their length (Fig. 5F), we are left with a strong peak parallel to the orientation of the mapped faults at 80°–85° (45° from the inferred orientation of σ_1). Overall the combined (weighted) rose plot is very similar to the rose plot of the weighted DEM lineament analysis, indicating that though the density of lineaments from the DEM analysis was low, their lengths helped them outweigh the smaller, lineament dense ASTER image. The potential of Riedel shears also exists within the combined dataset (Fig. 5E/F).

With agreement between the DEM and ASTER lineament analyses – and their combined dataset – the spread for the inferred maximum paleostress orientation is between 115° and 130°, with a more likely orientation of 125°–130°. This is based on a dominant orientation of

A DEM Lineament Average Frequency

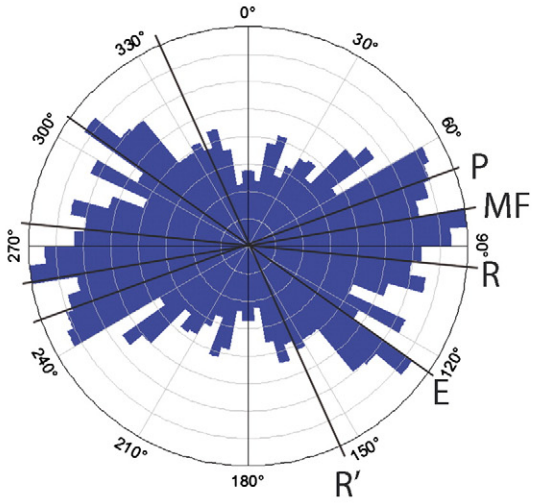

B DEM Lineament Average Frequency (weighted by length)

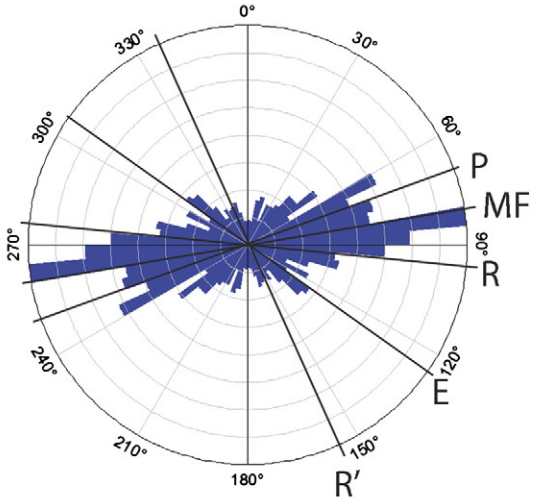

C ASTER Lineament Average Frequency

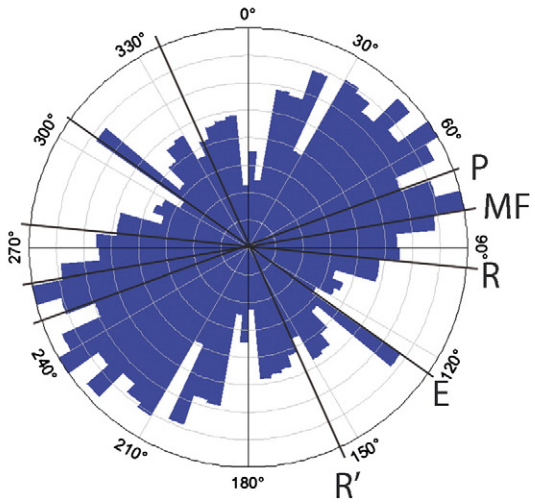

D ASTER Lineament Average Frequency (weighted by length)

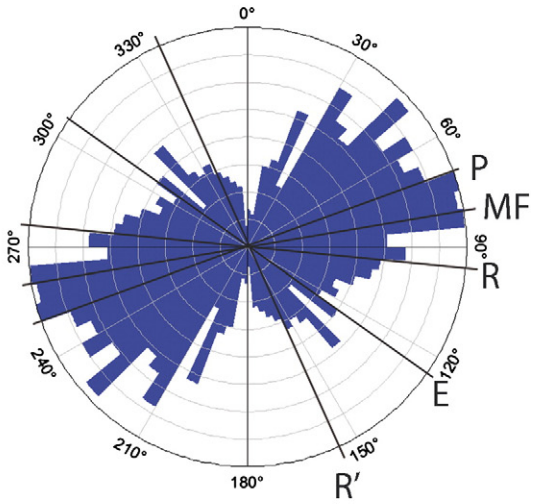

E Combined Lineament Average Frequency

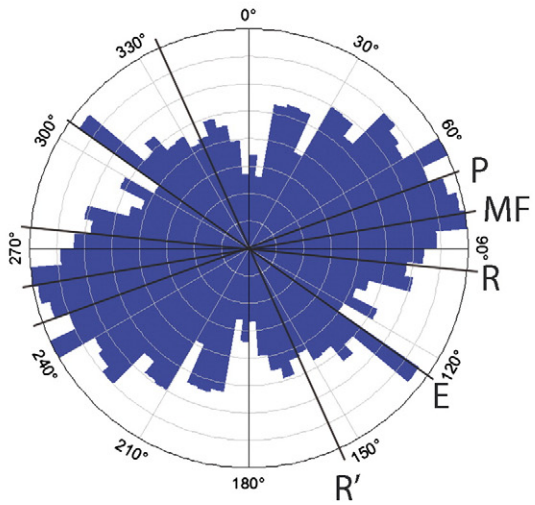

F Combined Lineament Average Frequency (weighted by length)

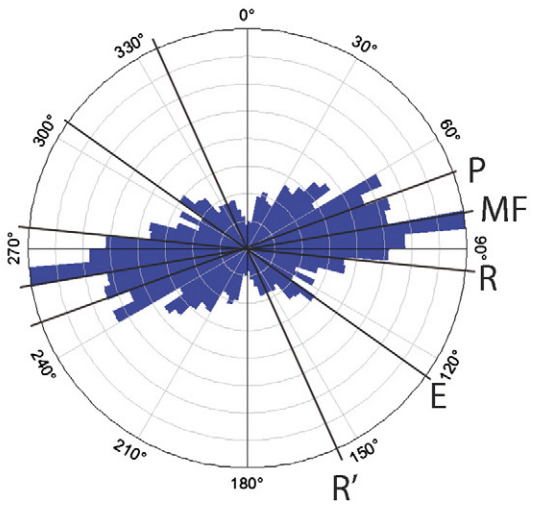

lineaments at around 80°–85° in the DEM and combined datasets, which correlates with the major orientation of mapped faults within the region. As a preliminary step to understanding the fault geometry in tectonically active areas with limited fault maps, we suggest that prominent features from a lineament analysis provide orientations that represent dominant fault populations. Thus, we can use the determined orientation for σ_1 from our lineament analyses to compare with the orientation of σ_1 based on the processed FEM to determine which model best represents the geometry of the through-going faults within the region.

6. Interpretation

To evaluate which of the two models best represents the active fault geometry, we compare the maximum principal stress axis orientations from the finite element method results with the inferred maximum principal stress axis from the lineament analysis. The maximum principal stress orientations of model 1 (115°–120°) and model 2 (120°–125°) have peaks that nearly coincide with the spread of inferred directions of σ_1 from the lineament analyses (115°–130°); however, model 2 results in a σ_1 orientation most close to the more likely orientation of 125°–130°. Model 1 shows a very large trend for σ_1 from 55°–60°. This orientation is located on the Armutlu–Almaçik block just south of the Düzce–Karadere fault portion of the northern strand, at which we would expect it to host a σ_1 orientation of 105°. To evaluate how this orientation occurred, we looked into the time series deformation of the blocks. As the blocks are pushed/pulled, the lack of a fault linking the bends in the northern and southern strands allows for the eastern part of the Armutlu–Almaçik zone to be pulled and distorted by the western portion of the Sakarya zone, subsequently rotating clockwise away from the Istanbul zone. This creates an extensional opening due to counterclockwise block rotation along the NE–SW trending portion of the northern strand (Düzce–Karadere Fault). Additionally, this unexpected σ_1 trend occurs as a dominant orientation from the center of the Armutlu–Almaçik block to the western most portion, particularly along the Iznik portion of the southern strand, at which we would expect a σ_1 orientation of 105° (based on the fault orientation). Model 2, displays only one principal stress orientation (120°–125°) that overlaps with the inferred orientation from the combined lineament analysis (115°–130°), and while model 2 shows a fan of principle stress orientations from 135° to 45°, when these orientations are weighted for magnitude, they are notably smaller than the peak centered between 135° and 95°. While there is still a peak at 55°–60°, the peak is rather small and distributed within the bodies of the blocks, rather than bounding the faults. Though the lineament analyses indicate that both models reproduce the inferred maximum stress orientation, the additional maximum stress orientations in the output of model 1 are not observed, indicating that model 2 is the most likely candidate for best representation of fault geometry. To confirm this we will compare the FEM stress orientation results with data from seismic events.

We collected thirty-four focal mechanism data (Fig. 2A) associated with several seismic events and/or their aftershocks (1943 Adapazarı–Hendek, 1957 Abant, 1967 Mudurnu, and 1999 Izmit earthquakes) located in our study area from the International Seismological Centre (International Seismological Centre, 2011) and the World Seismic Map (Heidbach et al., 2008). Data from these two sources are recordings from global stations. We determined the trend of the maximum principal stress axis, which is assumed to be synonymous with the P kinematic axis. Applying density contours to the P kinematic axes, we were able to procure a nearly horizontal (<5°) orientation for the regional P axis at approximately 125°. As this value is nearly horizontal, we can assume that the derived regional orientation of the P kinematic axis is synonymous to the orientation of the maximum horizontal stress. The orientation of 125° also matches the σ_1 orientation (low to no plunge) determined by Kiratzi (2002), Bohnhoff et al. (2006), and Örgülü (2011). This orientation falls within the range for the orientation of maximum principal stress determined from both FEM models. To further analyze the focal mechanism data, we looked at each focal mechanism separately and compared it to the immediate FEM stress orientations from both models within a buffer of 10 km around the epicenter. While both models exhibited stress orientation values similar to the individual focal mechanisms they corresponded to, Model 1 orientations showed the greatest deviation from focal mechanism orientations of σ_1, particularly along the Düzce–Karadere fault. Deviations from the focal mechanism data can be associated with the comparison of 3D focal mechanisms, with 2D model results. In the latter, orientations are assumed to have no plunge, and this could subsequently increase the deviation of model stress orientations as compared to focal mechanisms, especially when focal mechanism P-axis attitudes exhibit a plunge greater than 30°. In addition, the majority of focal mechanisms are deeper than what the 2D model represents, which is the upper 0.5–1.0 km of crust. The focal mechanisms of the earthquakes are as deep as 15 km, at which point the fault geometry could potentially vary. However, based on the smaller deviation exhibited, model 2 best represents the fault geometry within the region.

7. Conclusion

The methodology presented in this paper can be used to remotely identify approximate active fault geometries, which may not have well-developed surface expressions. Through an integrative approach of stress modeling with remote sensing techniques, the active fault geometry with the linking fault in model 2 best explains the primary stress orientations as observed from deformation patterns and earthquake focal mechanisms within the region of interest. The absence of a linking fault (model 1) led to multiple maximum stress orientations not evident in the inferred paleostress or earthquake focal mechanism data, and is attributed to clockwise rotation away from the Istanbul zone of the eastern Armutlu–Almaçik zone as its western portion pulled and distorted it. The presence of the linking fault in the model removes distortion, and allows for transfer of displacement, thus playing an important role in the development of the regional stress field. Although the valley in the southern portion of the Mudurnu region has previously been interpreted to host a fault with both extensional and strike-slip kinematics based on both topographic and seismic data (Armijo et al., 1999; engör et al., 2005), we show that it continues northward and it is an important linking feature of the NAF system. As a linking structure, this fault must be a significant component in future models of the NAF system in this region. It is predicted to facilitate long-term slip transfer and future modeling will help determine if the linking structure impedes or facilitates earthquake rupture propagation.

References

Aagaard, B., Kientz, S., Knepley, M., Strand, L., Williams, C., 2012. PyLith user manual, version 1.7.1. Comput. Infrastruct. Geodyn.

Akşay, A., Şükrü, P., Gedik, I., Bilginer, E., Duru, M., Akbaş, B., Altun, I., 2002. Zonguldak. In: Şenel, M. (Ed.), Türkiye Jeoloji Haritası.

Akyüz, H.S., Hartleb, R., Barka, A., Altunel, E., Sunal, G., Meyer, B., Armijo, R., 2002. Surface rupture and slip distribution of the 12 November 1999 Düzce earthquake (M7.1), North Anatolian Fault, Bolu, Turkey. Bull. Seismol. Soc. Am. 92, 61–66.

Ambraseys, N.N., Zatopek, A., 1969. The Mudurnu Valley, West Anatolia, Turkey, earthquake of 22 July 1967. Bull. Seismol. Soc. Am. 59, 68.

Armijo, R., Meyer, B., Hubert, A., Barka, A., 1999. Westwards propagation of the North Anatolian Fault into the Northern Aegean: timing and kinematics. Geology 27, 267–270.

Fig. 5Rose-diagrams of lineament orientation frequencies and length-weighted frequencies for (A, B) the DEM lineament analysis, (C, D) the ASTER image lineament analysis, and (E, F) a combined lineament analysis. North is at 0°. Riedel Shears (R and R′) are imposed on the images with the "main fault" (MF) at 80°. P shears are labeled with "P", and "E" represents the extensional fracture orientations. North is at 0°.

Armijo, R., Meyer, B., Navarro, S., King, G., 2002. Slip partitioning in the Sea of Marmara pull-apart: a clue to propagation processes of the North Anatolian Fault. Terra Nova 14, 80–86.

Barka, A.A., 1992. The North Anatolian fault zone. Ann. Tectonicae 6, 164–195 (Suppl.).

Barka, A.A., Kadinsky-Cade, K., 1988. Strike-slip fault geometry in Turkey and its influence on earthquake activity. Tectonics 7, 663–684.

Barka, A., Akyüz, H.S., Altunel, E., Sunal, G., Çakir, Z., Dikbas, A., Yerli, B., Armijo, R., Meyer, B., de Chabalier, J.B., Rockwell, T., Dolan, J.R., Hartleb, R., Dawson, T., Christofferson, S., Tucker, A., Fumal, T., Langridge, R., Stenner, H., Lettis, W., Bachhuber, J., Page, W., 2002. The surface rupture and slip distribution of the 17 August 1999 Izmit earthquake (M7.4), North Anatolian Fault. Bull. Seismol. Soc. Am. 92, 43–60.

Barton, N., 2007. Rock Quality, Seismic Velocity, Attenuation and Anisotropy. Taylor & Francis/Balkema, Leiden, The Netherlands.

Bell, F.G., 2007. Basic Environmental and Engineering Geology. Whittles Publishing Limited, Dunbeath, Scotland.

Ben-Zion, Y., Peng, Z., Okaya, D., Seeber, L., Armbruster, J.G., Ozer, N., Michael, A.J., Baris, S., Aktar, M., 2003. A shallow fault-zone structure illuminated by trapped waves in the Karadere–Düzce branch of the North Anatolian Fault, western Turkey. Geophys. J. Int. 152, 699–717.

Bilham, R., King, G., 1989. The morphology of strike-slip faults: examples from the San Andreas Fault, California. J. Geophys. Res. 94, 10204–10216.

KOERI-UDIM, 2012. Historical earthquakes catalog. In: Centre, B.U.K.O.a.E.R.I.-N.E.M. (Ed.), Istanbul, Turkey.

Bohnhoff, M., Grosser, H., Dresen, G., 2006. Strain partitioning and stress rotation at the North Anatolian fault zone from aftershock focal mechanisms of the 1999 Izmit Mw = 7.4 earthquake. Geophys. J. Int. 166, 12.

Bohnhoff, M., Bulut, F., Dresen, G., Malin, P.E., Eken, T., Aktar, M., 2013. An earthquake gap south of Istanbul. Nat. Commun. 4.

Bowman, D.D., King, G.C.P., 2001. Accelerating seismicity and stress accumulation before large earthquakes. Geophys. Res. Lett. 28, 4039–4042.

Boyd, T.M., 2003. Density variations of earth materials. In: Thomas, L. (Ed.), Introduction to Geophysical Exploration, Gravity Module, University of Melbourne.

Byerlee, J., 1978. Friction of rocks. Pageoph 116, 615–626.

Davis, G.H., 1999. Structural geology of the Colorado plateau region of southern Utah, with special emphasis on deformation bands. Geol. Soc. Am. Spec. Pap. 342, 1–157.

Dewey, J.F., engör, A.M.C., 1979. Aegean and surrounding regions: complex multiplate and continuum tectonics in a convergent zone. Geol. Soc. Am. Bull. 90, 84–92.

Dewey, J.F., Hempton, M.R., Kidd, W.S.F., Şaroğlu, F., Şengör, A.M.C., 1986. Shortening of continental lithosphere: the neotectonics of eastern Anatolia–a young collision zone. In: Coward, M.P., Ries, A.C. (Eds.), Collision Tectonics. Geol. Soc. Lond. Spec. Publ. pp. 3–36.

DU/GSC, 2001. Database of global rock properties. In: Laboratory, D.U.G.S.o.C.H.P. (Ed.), Halifax, Nova Scotia, Canada.

Ergintav, S., Burgmann, R., McClusky, S., Cakmak, R., Reilinger, R., Lenk, O., Barka, A., Ozener, H., 2002. Postseismic deformation near the Izmit earthquake (08/17/1999, M = 7.5) rupture zone. Bull. Seismol. Soc. Am. 92, 194–207.

Gülen, L., Pinar, A., Kalafat, D., Ozel, N., Horasan, G., Yilmazer, M., Isikara, A.M., 2002. Surface fault breaks, aftershock distribution, and rupture process of the 17 August 1999 Izmit, Turkey, earthquake. Bull. Seismol. Soc. Am. 92, 230–244.

Heidbach, O., Tingay, M., Barth, A., Reinecker, J., Kurfeß, D., Müller, B., 2008. The World Stress Map Database Release.

Hergert, T., Heidbach, O., 2010. Slip-rate variability and distributed deformation in the Marmara Sea fault system. Nat. Geosci. 132-135.

Hergert, T., Heidbach, O., 2011. Geomechanical model of the Marmara Sea region – II. 3-D contemporary background stress field. Geophys. J. Int. 185, 1090–1102.

Hisarli, M.Z., Çinku, M.C., Orbay, N., 2011. Paleomagnetic evidence of complex tectonic rotation pattern in the NW Anatolian region: implications for the tectonic history since the Middle Eocene. Tectonophysics 505, 13.

Hubert-Ferrari, A., Armijo, R., King, G.C.P., Meyer, B., Barka, A., 2002. Morphology, displacement and slip rates along the North Anatolian Fault (Turkey). J. Geophys. Res. 107, 1–33.

Hubert-Ferrari, A., King, G., Van Der Woerd, J., Villa, I., Altunel, E., Armijo, R., 2008. Long-term evolution of the North Anatolian fault (Turkey). Geol. Soc. Lond. Spec. Publ. 42.

International Seismological Centre, 2011. In: Cent, I.S. (Ed.), Thatcham, United Kingdom.

Jiménez-Munt, I., Sabadini, R., Gardi, A., 2006. Active deformation in the Mediterranean from Gibraltar to Anatolia inferred from numerical modelling and geodetic and seismological data. J. Geophys. Res. 108, 1–24.

Kasapoglu, K.E., Toksöz, M.N., 1983. Tectonic consequences of the collision of the Arabian and Eurasian plates: finite element models. Tectonophysics 100, 71–95.

King, G., 1986. Speculations on the geometry of the initiation and termination processes of earthquake rupture and its relation to morphology and geological structure. Pageoph 124, 567–585.

King, G., Nábělek, J., 1985. Role of fault bends in the initiation and termination of earthquake rupture. Science 228, 984–987.

Kiratzi, A.A., 2002. Stress tensor inversions along the westernmost North Anatolian Fault Zone and its continuation into the North Aegean Sea. Geophys. J. Int. 151, 360–376.

Koulakov, I., Bindi, D., Parolai, S., Grosser, H., Milkereit, C., 2010. Distribution of seismic velocities and attenuation in the crust beneath the North Anatolian Fault (Turkey) from local earthquake tomography. Bull. Seismol. Soc. Am. 100, 207–224.

Kröner, A., Stern, R.J., 2004. Pan-African orogeny. Encycl. Geol. 1, 1–12.

Le Pichon, X., Chamot-Rooke, N., Rangin, C., engör, A.M.C., 2003. The North Anatolian Fault in the Sea of Marmara. J. Geophys. Res. 108, 2179–2198.

Lesne, O., Calais, E., Deverchére, J., 1998. Finite element modelling of crustal deformation in the Baikal rift zone: new insights into the active–passive rifting debate. Tectonophysics 289, 327–340.

McClusky, S., Balassanian, S., Barka, A., Demir, C., Ergintav, S., Georgiev, I., Gurkan, O., Hamburger, M., Hurst, K., Kahle, H., Kastens, K., Kekelidze, G., King, R., Kotzev, V., Lenk, O., Mahmoud, S., Mishin, A., Nadariya, M., Ouzounis, A., Paradissis, D., Peter, Y., Prilepin, M., Reilinger, R., Sanli, I., Seeger, H., Tealeb, A., Toksöz, M.N., Veis, G., 2000. Global positioning system constraints on plate kinematics and dynamics in the eastern Mediterranean and Caucasus. J. Geophys. Res. Solid Earth 105, 5695–5719.

McElfresh, S.B.Z., Harbert, W., Ku, C.-Y., Lin, J.-S., 2002. Stress modeling of tectonic blocks at Cape Kamchatka, Russia using principal stress proxies from high-resolution SAR: new evidence for the Komandorskiy block. Tectonophysics 354, 239–256.

McKenzie, D., Jackson, J., 1983. The relationship between strain rates, crustal thickening, palaeomagnetism, finite strain and fault moments within a deforming zone. Earth Planet. Sci. Lett. 65, 182–202.

McQuarrie, N., Stock, J.M., Verdel, C., Wernicke, B.P., 2003. Cenozoic evolution of neothethys and implications for the causes of plate motions. Geophys. Res. Lett. 30.

Muller, J.R., Aydin, A., Maerten, F., 2003. Investigating the transition between the 1967 Mudurnu Valley and 1999 Izmit earthquakes along the North Anatolian fault with static stress changes. Geophys. J. Int. 154, 11.

Neugebauer, J., Löffler, M., Berkhemer, H., Yatman, A., 1997. Seismic observations at an overstep of the western North-Anatolian Fault (Abant–Sapanca region, Turkey). Int. J. Earth Sci. 86, 9.

Örgülü, G., 2011. Seismicity and source parameters for small-scale earthquakes along the splays of the North Anatolian Fault (NAF) in the Marmara Sea. Geophys. J. Int. 184, 385–404.

Özalaybey, S., Ergin, M., Aktar, M., Tapırdamaz, C., Biçmen, F., Yörük, A., 2002. The 1999 Izmit earthquake sequence in Turkey: seismological and tectonic aspects. Bull. Seismol. Soc. Am. 82, 376–386.

Ozener, H., Dogru, A., Unlutepe, A., 2009. An approach for rapid assessment of seismic hazards in Turkey by continuous GPS data. Sensors 9, 602–615.

Öztürk, K., Yaltirak, C., Alpar, B., 2009. The relationship between the tectonic setting of the Lake Iznik Basin and the middle strand of the North Anatolian Fault. Turk. J. Earth Sci. 18, 209–224.

Palyvos, N., Pantosti, D., Zabci, C., D'Addezio, G., 2007. Paleoseismological evidence of recent earthquakes on the 1967 Mudurnu Valley earthquake segment of the North Anatolian Fault. Bull. Seismol. Soc. Am. 97, 15.

Parsons, T., 2004. Recalculated probability of M ≥ 7 earthquakes beneath the Sea of Marmara, Turkey. J. Geophys. Res. 109.

Provost, A.-S., Chéry, J., Hassani, R., 2003. 3D mechanical modeling of the GPS velocity field along the North Anatolian fault. Earth Planet. Sci. Lett. 209, 361–377.

Reilinger, R., McClusky, S., Vernant, P., Lawrence, S., Ergintav, S., Cakmak, R., Ozener, H., Kadirov, F., Guliev, I., Stepanyan, R., Nadariya, M., Hahubia, G., Mahmoud, S., Sakr, K., ArRajehi, A., Paradissis, D., Al-Aydrus, A., Prilepin, M., Guseva, T., Evren, E., Dmitrotsa, A., Filikov, S.V., Gomez, F., Al-Ghazzi, R., Karam, G., 2006. GPS constraints on continental deformation in the Africa–Arabia–Eurasia continental collision zone and implications for the dynamics of plate interactions. J. Geophys. Res. Solid Earth 111 (B05411).

Riedel, W., 1929. Zur Mechanik geologischer Bruscherscheinungen: ein Beitrag zum Problem der "Fiederspälten". Centralblatt Mineral. Geol. Paläontol. B 14.

Scawthorn, C., Johnson, G.S., 2000. Preliminary report: Kocaeli (Izmit) earthquake of 17 August 1999. Eng. Struct. 22, 727–745.

Schwartz, D.P., Coppersmith, K., 1986. Seismic hazards: new trends in analysis using geologic data. Active Tectonics 215–230.

engör, A.M.C., 1979. The North Anatolian Transform Fault: its age, offset and tectonic significance. J. Geol. Soc. Lond. 136, 269–282.

engör, A.M.C., Canıtez, N., 1982. The North Anatolian Fault, Boulder, CO. Am. Geophys. Union. Geol. Soc, Washington, DC.

engör, A.M.C., Natal'in, B.A., 1996. Turkic-type orogeny and its role in the making of the continental crust. Annu. Rev. Earth Planet. Sci. 24, 263–337.

engör, A.M.C., Görür, N., aroğlu, F., 1985. Strike-slip Faulting and Related Basin Formation in Zones of Tectonic Escape: Turkey as a Case Study.

engör, A.M.C., Tüysüz, O., İmren, C., Sakinç, M., Eyidoğan, H., Görür, N., Le Pichon, X., Rangin, C., 2005. The North Anatolian Fault: a new look. Annu. Rev. Earth Planet. Sci. 33, 37–112.

Sibson, R.H., 1986. Earthquakes and lineament infrastructure. Philos. Trans. R. Soc. 317, 63–79.

Slemmons, D.B., Depolo, C.M., 1986. Evaluation of active faulting and associated hazards. Studies in Geophysics—Active Tectonics. National Academy Press, Washington, DC, pp. 45–62.

Stein, R.S., Barka, A.A., Dietrich, J.H., 1997. Progressive failure on the North Anatolian fault since 1939 by earthquake stress triggering. Geophys. J. Int. 128, 594–604.

USGS, 2008. GLSDEM tile for N040_E030, Global Land Survey Digital Elevation Model (GLSDEM). Global Land Cover Facility, University of Maryland, College Park, Maryland.

Wilcox, R.E., Harding, T.P., Seely, D.R., 1973. Basic wrench tectonics. Am. Assoc. Pet. Geol. Bull. 57, 22.

Yılmaz, Y., Tüysüz, O., Yiğitbaş, E., Genç, .C., engör, A.M.C., 1997. Geology and tectonic evolution of the Pontides. In: AAPG (Ed.), AAPG Memoir 68: Regional and Petroleum Geology of the Black Sea and Surrounding Region. AAPG, pp. 183–226.